Development of an Optical Sensor Capable of Measuring Distance, Tilt, and Contact Force

Takahiro Nozaki , *Member, IEEE,* and Hermano Igo Krebs, *Fellow, IEEE*

Abstract—Depth, proximity, and tactile sensors are often used in robotic object manipulation. The three types of sensors are combined to address each sensor limitation: Depth use is limited by blind spots and measurable range, proximity sensor is limited to millimetric distances, and the tactile sensor requires direct contact with the object. Here we present a novel sensor that can simultaneously measure millimetric distance and surface tilt, as well as contact force. We demonstrated the advantage of this novel sensor during a contact task. There, we implemented an admittance control and succeeded in achieving smooth transition from zero- to infinite-impedance contact condition and vice-versa. This novel sensor affords the realization of advanced interactions between robot and objects and contrary to previous approaches—limited by distance, blind spots, and impact force during initial contact—demonstrated good performance at all times with smooth and continuous measurements during contact.

Index Terms—Admittance control, contact force, haptics, impedance control, object manipulation, proximity sensor, robotics.

I. Introduction

VARIOUS types of sensors such as cameras, depth sensors, force sensors, and tactile sensors are used for object recognition and robotic object manipulation. Cameras and depth sensors are often used because they can instantaneously acquire information across a broad field of view. However, there are important shortcomings: The robot arm itself or obstacles can create blind spots [1], [2]. One can attempt to address the limitation by adding an additional set of cameras or depth sensors to the end effector. However, the additional vision system requires
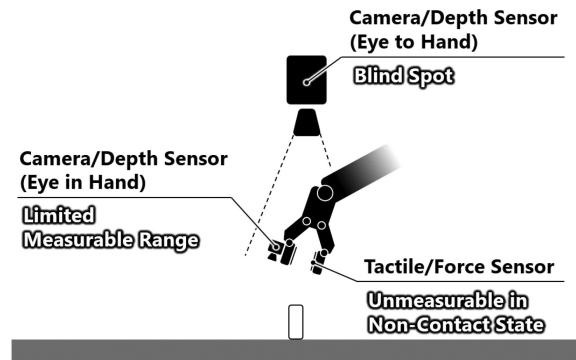

Fig. 1. Setup locations of cameras, depth sensors, tactile sensors, and force sensors and the disadvantages of each sensor.

additional time for image processing; moreover, its focal adjustment becomes difficult at short distances [3], [4]. Hence the utilization of proximity sensors to measure millimetric distance and detect contact are increasingly being adopted for use [5].

Meanwhile, force and tactile sensors are widely used during object manipulation to enable safer physical interaction between the robot and the environment [6]–[13]. Of notice, these sensors provide no information during noncontact phase. Often the combination of these three types of sensors is the "gold-standard" as it addresses each sensor's individual disadvantage but it comes with increased cost and complexity [14]–[16]. Fig. 1 summarizes different sensor arrangements and individual sensor disadvantages.

To overcome these disadvantages, Hughes *et al.* [17] proposed using a photo reflector, a type of proximity sensor, to estimate the force. The photo reflector has some disadvantages as the reflectance changes depending on the color and material of the object. Hughes shows the results for the classification of touch gesture, but not detailed results for accuracy. Koyama and colleagues proposed an alternative method of detecting contact that is insensitive to the object reflectance using the emission phase of a light-emitting diode. However, Koyama [18] did not show force response. Similarly, Tsuji [19] limited the influence of the object reflectivity using a time-of-flight type proximity sensor. Moreover, the force information is acquired by separately mounted piezoresistive pressure sensors [20].

We have been investigating the development of better sensors that combine depth sensing, proximity, and tactile capabilities. Here we introduce a novel sensor capable of simultaneously measuring distance, surface tilt, and contact force without being affected by the reflectivity of the object. We will describe its
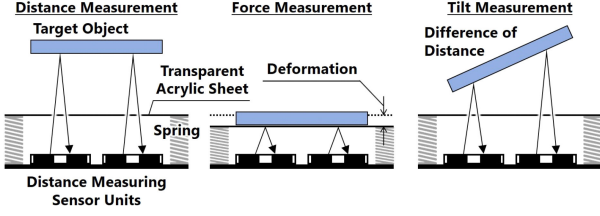
Fig. 2. Fundamental principles of the novel proximity sensor. The sensor is composed of multiple distance measuring sensor units, springs, and a transparent sheet and it is capable of simultaneously measuring distance, tilt, and contact force.
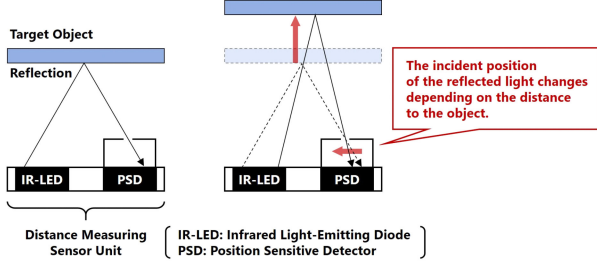

Fig. 3. Measurement principle of distance measuring sensor units. The distance measuring sensor units irradiate IR-LEDs and acquire the incident position of the reflected light showing the distance to the object through PSDs.

principle of operation and demonstrate its application during a contact task.

The remainder of this article is organized as follows: Section II introduces the basic principle of the novel sensor. Section III presents the detailed specifications of this sensor. Section IV presents the distance and tilt response, as well as the result of contact force measurement. The results of the contact task using this sensor are described in Section V and Section VI concludes the article.

II. BASIC PRINCIPLE OF THE NOVEL SENSOR

The basic principle of the novel optical sensor developed herein is shown in Fig. 2. The sensor is comprised of multiple distance measuring sensor units, springs, and a transparent sheet. Distance measuring sensor units are devices that measure the distance to the object by irradiating infrared rays from light-emitting diodes (IR-LEDs) and by acquiring the incident position of the reflected light showing geometric relationship with the object through position sensitive detectors (PSDs) as shown in Fig. 3. Since the PSDs derive the incident position from the distribution of the incident light intensity, it is possible to obtain the distance information to the target object almost unaffected by the reflectance of the object and ambient light. The sensor allows us to measure distance when the object is located farther than the equilibrium length of the springs. Meanwhile, if the object is closer than the equilibrium length of the springs, the sensor acts as a force sensor. Force information is calculated as follows:

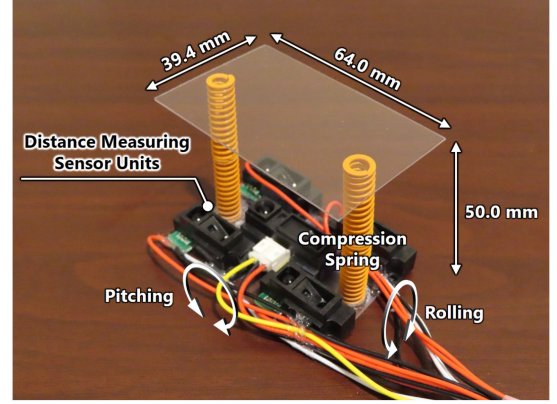$$f = k\left(x_{e} - x\right) \quad \text{if } (x < x_{e}). \tag{1}$$

Fig. 4. Appearance of the developed proximity sensor. The four units (Sharp Corporation, GP2Y0A21SK0F) mounted at each vertex of the rectangle measure distance, tilt, and contact force. Note a fifth unit (Sharp Corporation, GP2Y0A51SK0F) located at the center of the rectangle. This extra unit has the ancillary role of detecting the presence of an object within a larger range.

Here, k, x_{e}, and x denote the equivalent spring constant, the equilibrium length of the springs, and the position of the contact object, respectively. k and x_{e} are known material dependent quantities. In addition, the position response obtained from n PSDs is set as $x_{i}(1 \leq i \leq n)$, and the response m that expresses the gradient of the object by using the transformation matrix T corresponding to the geometric position of the PSD was as follows:

$$m = Tx \tag{2}$$

$$x = \begin{bmatrix} x_1 & \cdots & x_i & \cdots & x_n \end{bmatrix}^{T}. \tag{3}$$

In other words, information on the gradient of the object can be acquired by combining the responses of multiple PSDs.

III. SPECIFIC CONFIGURATION

Fig. 4 shows the appearance of the prototyped sensor. Transparent sheets were then mounted on the prototype via two springs, and their performances were confirmed. As four distance measuring sensor units are used in this prototype, the position responses are expressed as follows:

$$x = \begin{bmatrix} x_1 & x_2 & x_3 & x_4 \end{bmatrix}^{T}. \tag{4}$$

If the transformation matrix is set as follows:

$$T = \frac{1}{4} \begin{bmatrix} 1 & 1 & 1 & 1 \\ -1 & 1 & -1 & 1 \\ 1 & 1 & -1 & -1 \\ 1 & -1 & -1 & 1 \end{bmatrix} \tag{5}$$

the converted response is

$$m = \begin{bmatrix} m_1 & m_2 & m_3 & m_4 \end{bmatrix}^{T} = Tx. \tag{6}$$

Here, m_1, m_2, m_3, and m_4 are the values indicating the distance of the object, inclination of the pitch direction of the object, inclination of the roll direction of the object, bending of the object, respectively. These are hereinafter referred to as "distance mode," "pitching mode," "rolling mode," and "bending mode."
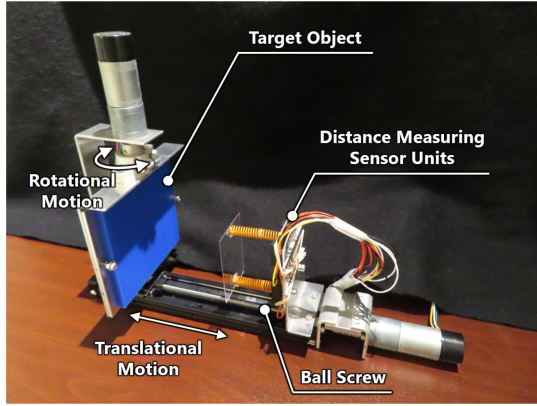
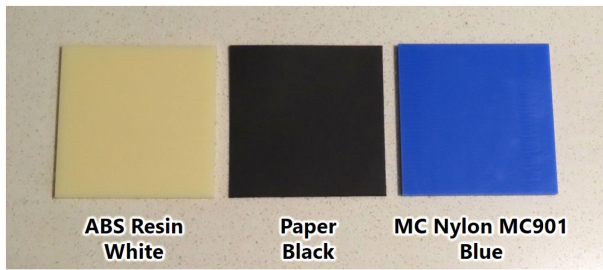Fig. 5.   Appearance of the developed proximity sensor.

Fig. 6.   Appearance of three plates with different colors and materials used as the target objects.

Similarly, for the output voltage of the sensor, each mode is defined as follows:

$$\boldsymbol{v} = [v_1 \ v_2 \ v_3 \ v_4]^{\mathrm{T}} = \boldsymbol{T}\boldsymbol{v}_{\mathrm{sensor}}. \tag{7}$$

The $\boldsymbol{v}_{\mathrm{sensor}}$ is the vector that consists of the output voltage of the distance measuring sensor units. The \boldmath v shows the response in the each mode resulting from the transformation.

The distance measuring sensor units were connected to a STMicroelectronics microcontroller (NUCLEO-F413ZH). The microcontroller clock was set to 100 MHz, and the response from each distance measuring sensor unit was acquired at a frequency of 100 kHz using direct memory access. We used a moving average of 1000 samples to suppress the effect of noise and the final response value (cutoff frequency) was approximately 44.3 Hz.

IV. FUNCTIONAL VERIFICATION

This section presents the verification results of the sensor's basic functions. The equipment used in the tests is shown in Fig. 5. This equipment can fix the developed sensor and the target objects vertically. The position and angle of the target object can be adjusted by the two dc motors and the ball screw.

A. Distance Measurement

A white acrylonitrile butadiene styrene (ABS) resin plate, a black paper, and a blue monomer cast nylon plate (MC Nylon, MC901) shown in the Fig. 6 were used as the target objects with different colors and materials. The relation between the object position and the output voltage of the distance measuring sensor
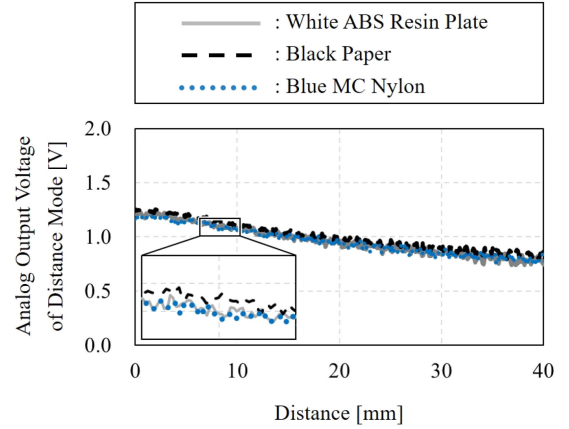

Fig. 7.   Relation between the distance to the object and the output voltage corresponding to the distance mode.

units corresponding to the distance mode response was recorded. The object was fixed parallel to the sensor and the distance was changed by the ball screw.

The measurement results are shown in the Fig. 7. The solid line, the dashed line, and the dotted line represent the responses when the object was the white ABS resin plate, the black paper, and the blue MC Nylon, respectively. The output voltage corresponding to the distance mode response decreased monotonically relative to the distance in all results.

By approximating all the results shown in the Fig. 7 with a quadratic function

$$\hat{x} = 57.88284v_1^2 - 199.99821v_1 + 159.13782, \tag{8}$$

is obtained. Here, the $\hat{x}$ and the v_1 represent the estimated distance and the output voltage corresponding to the distance mode response, respectively. Using this formula to estimate the distance to the object from the output voltage, the root mean square error (RMSE) was 2.787 mm.

B. Force Measurement

The ABS resin plate was placed in contact with the sensor, and force was applied to the ABS resin plate through a load cell and pushed in the direction to the sensor. The result is shown in Fig. 8. The solid line and the dashed line are the output voltage of the developed sensor corresponding to the distance mode response and the applied force measured by the load cell, respectively.

As a result of calculating the force response $\hat{f}$ from the output voltage of the sensor using the following linear function:

$$\hat{f} = 200v_1 - 248 \tag{9}$$

the RMSE was 0.966 N.

C. Tilt Measurement

The ABS resin plate was placed at 20 mm from the sensor, and the response was confirmed when the plate was tilted by the dc motor mounted on the top of the test equipment. The pitching mode response is shown in Fig. 9(a), and the rolling mode is shown in Fig. 9(b). The black line and the the light-colored line show the actual angle of the object measured by the rotary
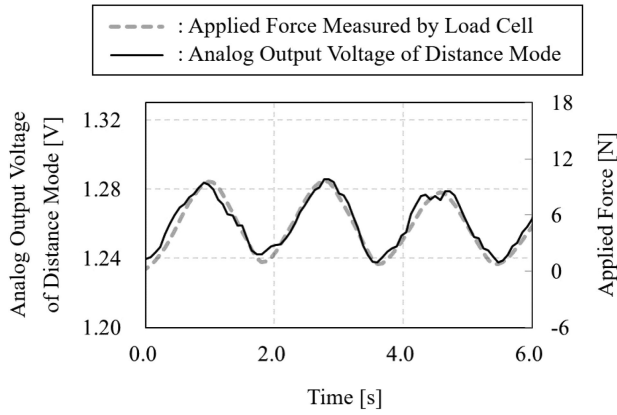
Fig. 8.   Relation between the applied force and the output voltage of the developed sensor corresponding to the distance mode response.
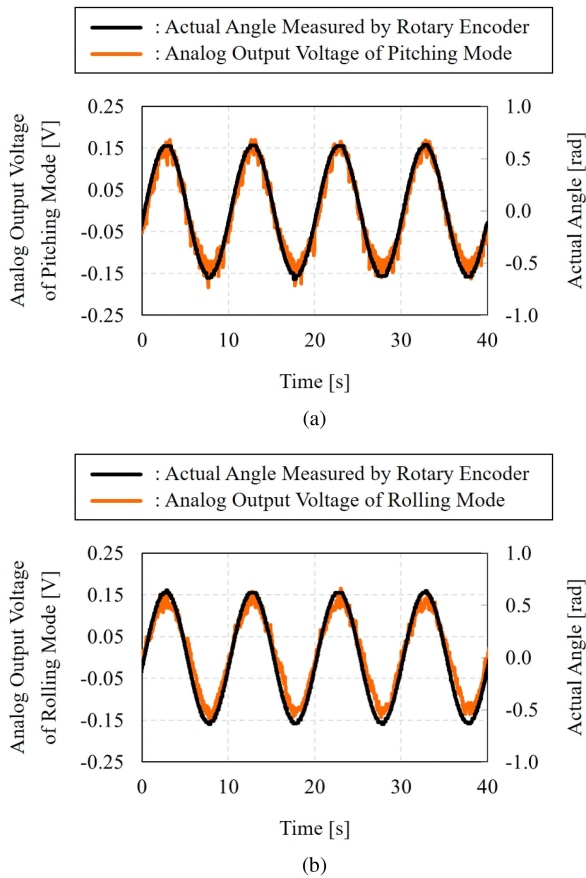

(a)

(b)

Fig. 9.   Relation between the angle and the output voltage of the developed sensor (a) Result of pitch angle. (b) Result of roll angle.

encoder attached to the dc motor and the output voltage in the pitching/rolling mode. By redrawing Figs. 9 and 10 is obtained. The θ and the φ mean the actual pitching angle and the rolling angle, respectively. The output voltage increased monotonically. The slope of the fitted straight line in the pitching mode was approximately 0.228, whereas the slope of the fitted line for the rolling mode was approximately 0.202. This difference is affected by the arrangement of the distance measuring sensor units located at each vertex of the rectangular sensor base.
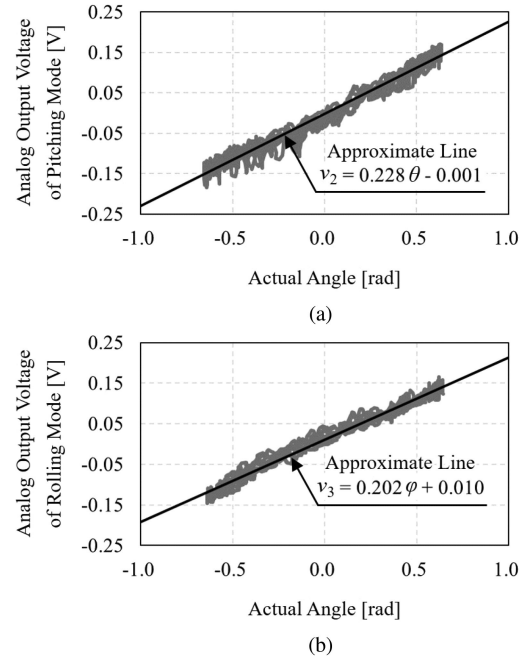

(a)

(b)

Fig. 10.   Object tilt measurement results. (a) Relation between pitch angle and pitching mode. (b) Relation between roll angle and rolling mode. Solid black lines denote the approximate straight lines.

As a result of calculating the angle from the sensor responses using the inverse functions of the approximate lines shown in the Fig. 10, the RMSE in the pitching angle was 0.102 rad and the error in the rolling angle was 0.099 rad.

V. ADMITTANCE CONTROL

In this section, we discuss the application of the sensor to illustrate a few advantages of the novel sensor. Admittance control [21]–[25] is a technique to control the apparent mechanical impedance at the port of interaction [26]–[29]. Admittance control is an extremely important approach in realizing advanced physical interaction between robots and objects or between robots and humans. This section discusses the applicability of the novel sensor to an admittance controller. The following three types of experiments were performed to demonstrate the utility of the novel sensor.

1) Distance Mode Experiment: Sensor was used to measure distance only and the signal was not used in the feedback controller.

2) Force Sensor Mode Experiment: Sensor was used to function exclusively as a force sensor.

3) Distance and Force Mode Experiment: An experiment was conducted where the distance and force functions were used for feedback control.

A. Experimental Setup

The configuration of the experimental setup is shown in Fig. 11. Sensor response is sent to the microcontroller (STMicro-electronics Co., NUCLEO-F413ZH) to calculate the feedback command signal. The corresponding current value was inputted to the motor driver (Maxon Motor, ESCON Module 24/2) and
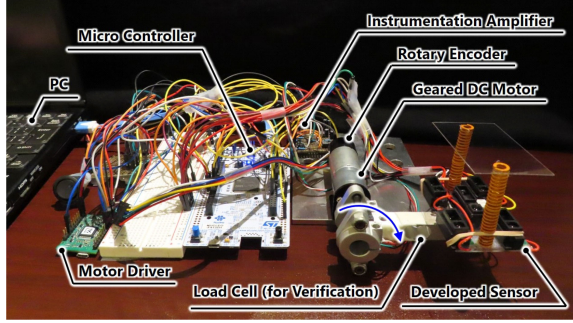
Fig. 11. Experimental device for impedance control using the developed sensor.
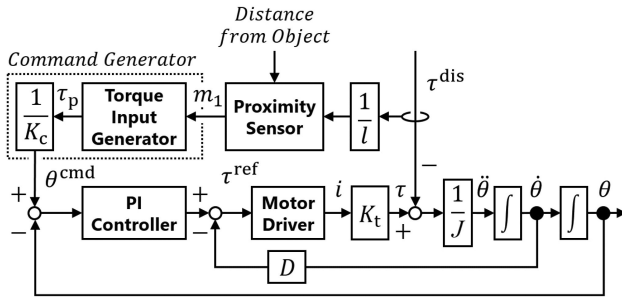

Fig. 12. Block diagram of admittance control.

the geared dc motor (reduction ratio of 1:98). The tilt response was obtained from encoders attached to the motor (resolution: 4704 counts per revolution). The load cell output was obtained with an instrumentation amplifier (LT1167cn8). This force measurement was collected for verification purposes and not used in the control loop.

B. Command of Admittance Control

Fig. 12 shows the block diagram of the implemented admittance control, where τ^{dis}, θ^{cmd}, τ^{ref}, i, τ, $\ddot{\theta}$, $\dot{\theta}$, θ, l, D, K_{t}, and K_{c} represent disturbance torque, angle command value of the motor, reference torque value, current, motor torque, angular acceleration, angular velocity, angle, link length, damping gain, torque constant, and desired stiffness coefficient.

Our sensor measures the approach to the target object and applied torque. The torque is divided by the desired stiffness and fed to internal proportional-integral position controller with an internal damping loop for stabilization. The calculation of the angle command is as follows.

1) *Tilt Command for the Distance Sensor Function Mode*: In this mode, although the sensor acquires the distance information to the object, the angle command value is zero

$$\theta^{\mathrm{cmd}} = 0. \quad (10)$$

2) *Tilt Command for the Force Sensor Function Mode:* In this mode, when the output voltage of the sensor is higher than a threshold, the commanded angle takes into consideration the applied torque and desired stiffness. During noncontact, when the sensor output is lower than the threshold, the angle command value is zero as in the

distance sensor function mode. The angle command value of the motor is calculated as

$$\theta^{\mathrm{cmd}} = \begin{cases} \dfrac{\tau_{\mathrm{p}}}{K_{\mathrm{c}}} = \dfrac{K_{\mathrm{f}}(m_1 - \lambda_1)}{K_{\mathrm{c}}} & (\lambda_1 < m_1) \\ 0 & (m_1 \le \lambda_1) \end{cases} \quad (11)$$

where λ_1 denotes the threshold that distinguishes between contact and noncontact condition. The K_{f} is the conversion coefficient from voltage to force, and the τ_{p} shows the torque of the admittance control.

3) *Tilt Command Value for Combined Distance and Force Sensor Function Mode:* In this mode, the command angle is calculated as:

$$\theta^{\mathrm{cmd}} = \begin{cases} \dfrac{\tau_{\mathrm{p}}}{K_{\mathrm{c}}} = \dfrac{K_{\mathrm{f}}(m_1 - \lambda_1)}{K_{\mathrm{c}}} & (\lambda_1 < m_1) \\[2mm] \dfrac{\tau_{\mathrm{p}}}{K_{\mathrm{c}}} = \dfrac{K_{\mathrm{f}}(m_1 - \lambda_2)}{K_{\mathrm{c}}} & (\lambda_2 < m_1 \wedge m_1 \le \lambda_1) \\[2mm] 0 & (m_1 \le \lambda_2) \end{cases} \quad (12)$$

where the λ_2 denotes the threshold that indicates when to start the torque command in a noncontact state. The torque command is generated even during noncontact by setting the λ_2 smaller than λ_1, where the motor rotates without any physical contact such as a human operator.

C. Experimental Results

Fig. 13 shows the experimental results. Fig. 13(a)–(c) are the force responses obtained by the load cell (used for verification purposes); Fig. 13(d)–(f) are the corresponding motor angle responses obtained from the encoders; Fig. 13(g)–(i) are the corresponding output voltage of the sensor in the distance mode. In each experiment, an object (white ABS resin plate) was brought closer to the sensor mounted at the link tip first without touching it twice and then pressing against it twice. In these experiments, the threshold λ_1 was set to 1.24 V, and the threshold λ_2 was set to 1.04 V, as shown by the dashed lines in Fig. 13(g)–(i). Fig. 13(g)–(i) shows that the target object approached four times in each experiment, the first two of which were noncontact and exceeded the threshold λ_2, and the second two were contact and exceeded the threshold λ_1.

Fig. 13(a)–(g) shows the force, angle, and sensor response, respectively, when the sensor is used as a distance sensor. Fig. 13(a) shows that an external force was applied at approximately 3.8 and 5.0 s. Fig. 13(d) shows that the motor angle variations due to external forces were small and the control of the stiffness was high. Incidentally, the angle command value is always zero in the experiment as described in (10). Therefore, this angle variation is caused by disturbance and is further suppressed by increasing the feedback gain and changing the sensitivity function.

Fig. 13(b)–(h) shows the force, angle, and sensor response, respectively, when the sensor is used as a force sensor. Similar to Fig. 13(a), it can be confirmed from Fig. 13(b) that the external force is applied at approximately 4.2 and 5.5 s. Fig. 13(e) also shows that the controlled stiffness is low, and flexible operations
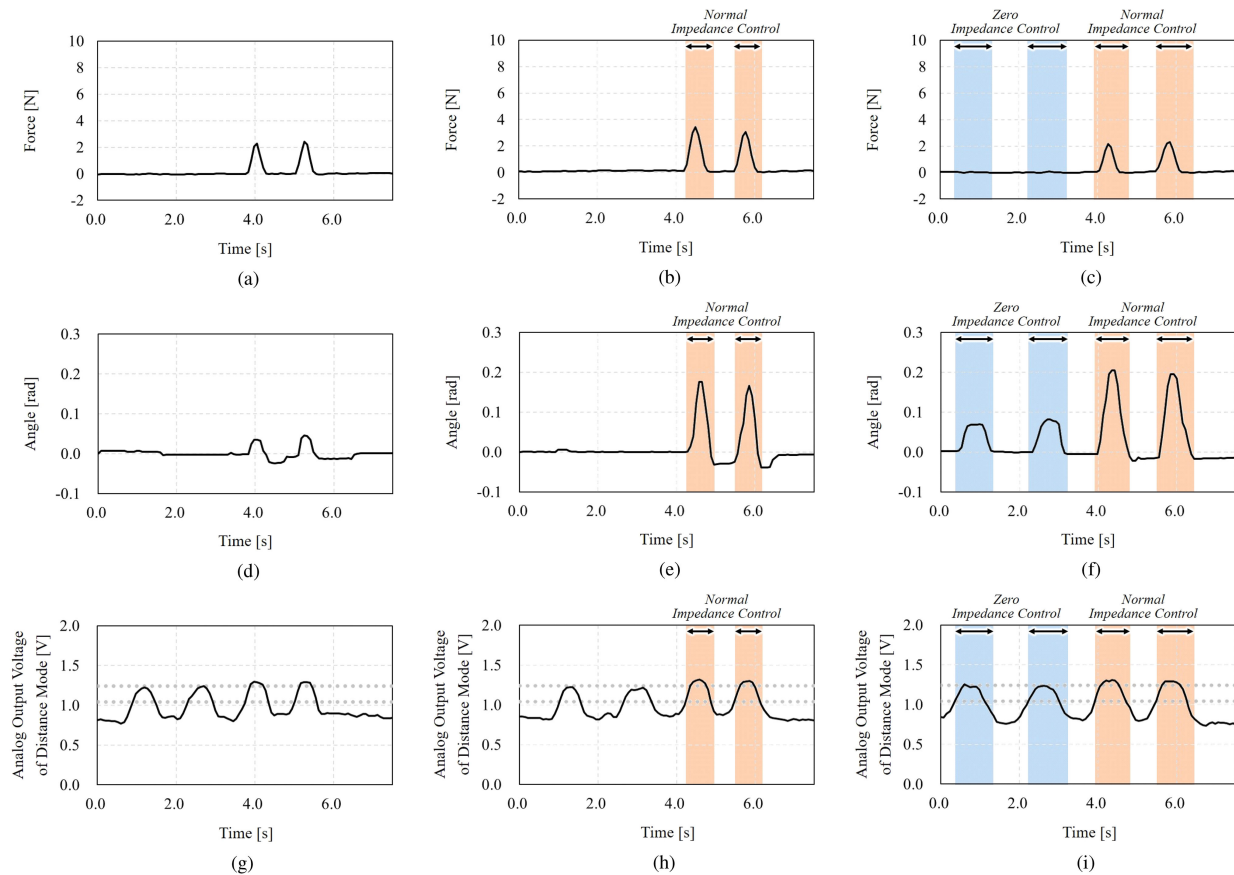
Fig. 13. Experimental results using the developed sensor. (a) Force response when only the distance sensor function of the sensor is used. (b) Force response when only the force sensor function of the sensor is used. (c) Force response when using both distance sensor function and force sensor function of the sensor. (d) Angle response when only the distance sensor function of the sensor is used. (e) Angle response when only the force sensor function of the sensor is used. (f) Angle response when using both distance sensor function and force sensor function of the sensor. (g) Analog voltage output in distance mode when only the distance sensor function of the sensor is used. (h) Analog voltage output in distance mode when only the force sensor function of the sensor is used. (i) Analog voltage output in distance mode when using both distance sensor function and force sensor function of the sensor.

were achieved due to the large angle variations produced, when compared to Fig. 13(d). This is because the angle command value is adjusted according to (11) depending on the applied external force.

Fig. 13(c)–(i) show the force, angle, and sensor response, respectively, when both the distance and force sensor functions of the novel sensor were used. Similar to Fig. 13(a) and (b), it can be confirmed from Fig. 13(c) that the external force was applied at approximately 4.0 and 5.5 s. Fig. 13(f) also shows that the motor angle changed when the object approached (approximately at 0.5 and 2.3 s) and when an external force was applied (approximately at 4.0 and 5.5 s). The novel sensor functioned initially as a distance sensor (from 0 to 3.6 s), and the angle command value is updated according to the distance from the object, see (12). The sensor functioned as a force sensor in the latter half (from 3.6 to 7.5 s), and a flexible and safe operation with low stiffness similar to that observed via Fig. 13(b) and (e) was observed.

In particular, it can be confirmed that the zero-impedance state was achieved around 0.5 and 2.3 s, where the motor rotated in response to the approach of the object, even though no force was applied to the sensor. It can also be seen that the distance measurement and force measurement were performed
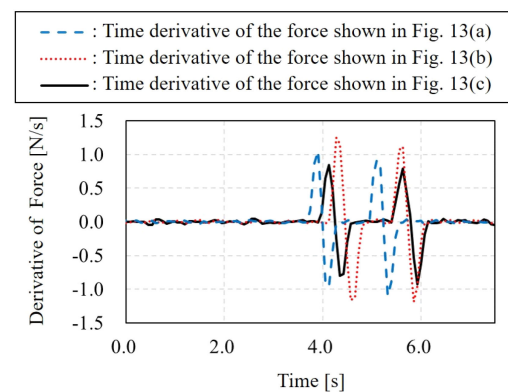
Fig. 14. Comparison of the time derivative of the force.

continuously, and the transition between the zero-impedance state and the normal impedance control state was smooth.

Fig. 14 shows a comparison between the time derivatives of the force shown in Fig. 13(a)(c). Note that the torque input shown in (12), which is generated in the noncontact state, suppressed the sudden change in force and reduced the impact at the onset of contact.

VI. Conclusion

In this article, we present a novel sensor that can simultaneously measure distance, tilt, and contact force. Results demonstrated that it is possible to measure these desired information regardless of the color and material of the target object. The RMSEs of distance, force, and tilt calculated from the output voltage of the sensor were 2.787 mm, 0.966 N, 0.102 rad in pitching rotation, and 0.099 rad in rolling rotation, respectively. Furthermore, we demonstrated the advantages of the sensor in a contact task employing an admittance controller. Results showed that we can modulate the stiffness using the novel sensor response. We used the distance information to achieve a zero impedance that enables motor operation in a noncontact case as well as a smooth transition to the desired impedance at contact. This novel sensor operated both as a proximity and force sensor. It was quite advantageous when the robot was expected to manipulate and handle objects. This article focused on the description of the sensor and its validation.

Another possible advantage of this sensor is its cost. We spent $70 (US dollars) purchasing the components in single units and speculate that the bulk cost could be a fraction of that. A further advantage of this sensor is its durability, which depends solely on the material and thickness of the transparent plate. While this sensor is very simple and robust, it is best to specify this interface based on the dynamic range of the expected contact forces. While further validation tests are expected prior to any commercial launch, we have confirmed the responsiveness of our alpha-prototype sensor after submitting it to over 1000 loading cycles.

We anticipate further work integrating it with more advanced control schemes, particularly to reduce the impact force at the contact. Further miniaturization of the sensor is expected. Although our prototype dimensions are $64 \times 39.4 \times 50$ mm, we estimate that the final dimensions might be of the order of $30 \times 20 \times 15$ mm (length, width, height) once we employ surface-mounted components and tighter design of the optical path and LED emission timing.

References

[1] G. Flandin, F. Chaumette, and E Marchand, "Eye-in-hand/eye-to-hand cooperation for visual servoing," in *Proc. IEEE Int. Conf. Robot. Autom.*, vol. 3, Apr. 2000, pp. 2741–2746.

[2] Z. Qiu, S. Hu, and X. Liang, "Model predictive control for uncalibrated and constrained image-based visual servoing without joint velocity measurements," *IEEE Access*, vol. 7, pp. 73540–73554, Jun. 2019.

[3] N. P. Papanikolopoulos, P. K. Khosla, and T. Kanade, "Visual tracking of a moving target by a camera mounted on a robot: A combination of control and vision," *IEEE Trans. Robot. Autom.*, vol. 9, no. 1, pp. 14–35, Feb. 1993.

[4] W. Pan, M. Lyu, K.-S. Hwang, M.-Y. Ju, and H. Shi, "A neuro-fuzzy visual servoing controller for an articulated manipulator," *IEEE Access*, vol. 6, pp. 3346–3357, Jan. 2018.

[5] K. Koyama, M. Shimojo, T. Senoo, and M. Ishikawa, "High-speed high-precision proximity sensor for detection of tilt, distance, and contact," *IEEE Robot. Autom. Lett.*, vol. 3, no. 4, pp. 3224–3231, Oct. 2018.

[6] Y. Bekiroglu, J. Laaksonen, J. A. Jorgensen, V. Kyrki, and D. Kragic, "Assessing grasp stability based on learning and haptic data," *IEEE Trans. Robot.*, vol. 27, no. 3, pp. 616–629, Jun. 2011.

[7] S. Cremer, S. K. Das, I. B. Wijayasinghe, D. O. Popa, and F. L. Lewis, "Model-free online neuroadaptive controller with intent estimation for physical human–robot interaction," *IEEE Trans. Robot.*, vol. 36, no. 1, pp. 240–253, Feb. 2010.

[8] R. Li and H. Qiao, "A survey of methods and strategies for high- precision robotic grasping and assembly tasks-some new trends," *IEEE/ASME Trans. Mechatronics*, vol. 24, no. 6, pp. 2718–2732, Dec. 2019.

[9] M. Costanzo, G. D. Maria, and C. Natale, "Two-fingered in-hand object handling based on force/tactile feedback," *IEEE Trans. Robot.*, vol. 36, no. 1, pp. 157–173, Feb. 2020.

[10] R. Calandra *et al.*, "More than a feeling: learning to grasp and regrasp using vision and touch," *IEEE Robot. Autom. Lett.*, vol. 3, no. 4, pp. 3300–3307, Oct. 2018.

[11] W. Yuan, S. Dong, and E. H. Adelson, "GELSIGHT: High-resolution robot tactile sensors for estimating geometry and force," *Sensors*, vol. 17, no. 12, Nov. 2017, Art. no. 2762.

[12] J. A. Fishel and G. E. Loeb, "Sensing tactile microvibrations with the BioTac-comparison with human sensitivity," in *Proc. IEEE RAS/EMBS Int. Conf. Biomed. Robot. Biomechatronics*, 2012, pp. 1122–1127.

[13] R. D. P. Wong, R. B. Hellman, and V. J. Santos, "Spatial asymmetry in tactile sensor skin deformation aids perception of edge orientation during haptic exploration," *IEEE Trans. Haptics*, vol. 7, no. 2, pp. 191–202, Jun. 2014.

[14] D. D. Gregorio, R. Zanella, G. Palli, S. Pirozzi, and C. Melchiorri, "Integration of robotic vision and tactile sensing for wire-terminal insertion tasks," *IEEE Trans. Autom. Sci. Eng.*, vol. 16, no. 2, pp. 585–598, Apr. 2019.

[15] N. Fazeli, M. Oller, J. Wu, Z. Wu, J. Tenenbaum, and A. Rodriguez, "See, feel, ACT: Hierarchical learning for complex manipulation skills with multisensory fusion," *Sci. Robot.*, vol. 4, no. 26, Jan. 2019, Art. no. eaav3123.

[16] M. A. Lee *et al.*, "Making sense of vision and touch: Learning multimodal representations for contact-rich tasks," *IEEE Trans. Robot.*, vol. 36, no. 3, pp. 582–596, Jun. 2020.

[17] D. Hughes, J. Lammie, and N. Correll, "A robotic skin for collision avoidance and affective touch recognition," *IEEE Robot. Autom. Lett.*, vol. 3, no. 3, pp. 1386–1393, Jul. 2018.

[18] K. Koyama, K. Murakami, T. Senoo, M. Shimojo, and M. Ishikawa, "High-speed, small-deformation catching of soft objects based on active vision and proximity sensing," *IEEE Robot. Autom. Lett.*, vol. 4, no. 2, pp. 578–585, Apr. 2019.

[19] S. Tsuji and T. Kohama, "Proximity skin sensor using time-of-flight sensor for human collaborative robot," *IEEE Sensors J.*, vol. 19, no. 14, pp. 5859–5864, Jul. 2019.

[20] J. Liang, J. Wu, H. Huang, W. Xu, B. Li, and F. Xi, "Soft sensitive skin for safety control of a nursing robot using proximity and tactile sensors," *IEEE Sensors J.*, vol. 20, no. 7, pp. 3822–3830, Apr. 2020.

[21] N. Hogan, "*Impedance control: An approach to manipulation: Part I-Theory; Part II-Implementation; Part III-Applications*," *ASME J. Dyn. Syst., Meas. Control*, vol. 107, pp. 1–24, Mar. 1985.

[22] S. A. Schneider and R. H. Cannon Jr, "Object impedance control for cooperative manipulation: Theory and experimental," *IEEE Trans. Robot. Autom.*, vol. 8, no. 3, pp. 383–394, Jun. 1992.

[23] A. Dietrich and C. Ott, "Hierarchical impedance-based tracking control of kinematically redundant robots," *IEEE Trans. Robot.*, vol. 36, no. 1, pp. 204–221, Feb. 2020.

[24] D. Kim, K. Koh, G.-R. Cho, and L.-Q. Zhang, "A robust impedance controller design for series elastic actuators using the singular perturbation theory," *IEEE/ASME Trans. Mechatronics*, vol. 25, no. 1, pp. 164–174, Feb. 2020.

[25] T. Nozaki, S. Shimizu, T. Murakami, and R. Oboe, "Impedance field expression of bilateral control for reducing data traffic in haptic transmission," *IEEE Trans. Ind. Electron.*, vol. 66, no. 2, pp. 1142–1150, Feb. 2019.

[26] P. H. Chang and S. H. Kang, "Stochastic estimation of human arm impedance under nonlinear friction in robot joints: A model study," *J. Neurosci. Meth.*, vol. 189, no. 1, pp. 97–112, May 2010.

[27] J. J. Palazzolo, M. Ferraro, H. I. Krebs, D. Lynch, B. T. Volpe, and N. Hogan, "Stochastic estimation of arm mechanical impedance during robotic stroke rehabilitation," *IEEE Trans. Neural. Syst. Rehabil.*, vol. 15, no. 1, pp. 94–103, Mar. 2007.

[28] T. Nozaki, T. Mizoguchi, and K. Ohnishi, "Motion expression by elemental separation of haptic information," *IEEE Trans. Ind. Electron.*, vol. 61, no. 11, pp. 6192–6201, Nov. 2014.

[29] P. H. Chang, K. Park, S. H. Kang, H. I. Krebs, and N. Hogan, "Stochastic estimation of human arm impedance using robots with nonlinear frictions: An experimental validation," *IEEE/ASME Trans. Mechatronics*, vol. 18, no. 2, pp. 775–786, Apr. 2013.
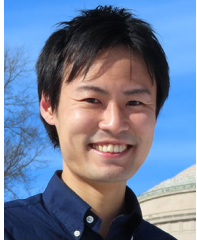
Takahiro Nozaki (Member, IEEE) received the B.E., M.E., and Ph.D. degrees from Keio University, Yokohama, Japan, in 2010, 2012, and 2014, respectively.

In 2014, he joined Yokohama National University, Yokohama, Japan, as a Research Associate. In 2015, he joined the Keio University, where he is currently an Assistant Professor. He was also a Visiting Scientist with Massachusetts Institute of Technology, Cambridge, MA, USA, from 2019 to 2021.

Dr. Nazoki was the recipient of the IEEE Industrial Electronics Society Under 35 Innovators Contest in 2019.

Hermano Igo Krebs (Fellow, IEEE) received the electrician degree in 1976 from Escola Tecnica Federal de Sao Paulo, Brazil, the B.S. and M.S. degrees in naval engineering from University of Sao Paulo, Brazil, in 1980 and 1987, respectively. He received another M.S. degree in ocean engineering from Yokohama National University, Japan, in 1989, and the Ph.D. degree in engineering from the Massachusetts Institute of Technology (MIT), Cambridge, in 1997.

He has been a Principal Research Scientist at MIT's Mechanical Engineering Department since 1997. He holds an affiliate position as an Adjunct Professor at University of Maryland School of Medicine, Neurology, as a Visiting Professor at Fujita Health University, Physical Medicine and Rehabilitation (Japan), at Osaka University, Mechanical Science and Bioengineering (Japan), and at Loughborough University, Wolfson School of Engineering (UK).

He is a Fellow of the IEEE and was nominated to this distinguished status "for contributions to rehabilitation robotics and the understanding of neuro-rehabilitation." He received "The 2009 Isabelle and Leonard Goldenson Technology and Rehabilitation Award," from the CPIRF; the 2015 IEEE-INABA Technical Award for Innovation leading to Production "for contributions to medical technology innovation and translation into commercial applications for Rehabilitation Robotics;" and he was selected as an IEEE-EMBS Distinguished Lecturer in 2021. He was one of the founders and Chairman of the Board of Directors of Interactive Motion Technologies from 1998 to 2016. He sold it to Bionik Laboratories, where he served as its Chief Science Officer and on the Board of Directors until July 2017. He later founded 4Motion Robotics.